5 Damping Ring

5.1 Introduction

Damping rings are necessary to reduce the emittances produced by the particle sources to the small values required for the linear collider. Emittance reduction is achieved via the process of radiation damping, i.e. the combination of synchrotron radiation in bending fields with energy gain in RF cavities. The design of the damping ring has to ensure a small emittance and a sufficient damping rate.

One of the main design criteria for the damping ring comes from the long beam pulse: a 1 ms pulse containing 2820 bunches, corresponding to an approximately 300 km long bunch train. To keep the damping ring length reasonable, the bunch train has to be stored in a compressed mode with a much smaller bunch spacing than in the rest of the accelerator. Consequently each bunch has to be individually injected and ejected. The ring length is then given by the bandwidth of the injection and extraction system. A bandwidth of 50 MHz (bunch spacing of 20 ns) requires a ring length of 17 km. To avoid the cost for an additional 17 km of ring tunnel, most of the damping ring will be in the form of straight sections installed in the linac tunnel [1]. Short return arcs requiring additional tunnels provide about 12 % of the circumference.

The ring energy is 5 GeV; this is a compromise between the need for higher energy to reduce space charge effects (see section 5.3.1) and damping wiggler costs, and a preferable lower energy which reduces the RF power needs and eases the design of the damping ring arcs.

The design of low emittance arcs with sufficiently high bending fields to provide enough damping becomes increasingly difficult at higher energies: thus the majority of the damping (95%) is supplied by long damping wigglers. The final extracted transverse emittance (ε_f) is given by

$$\varepsilon_f = \varepsilon_{eq} + (\varepsilon_f - \varepsilon_{eq})e^{-2T/\tau_D}$$

where ε_i and ε_{eq} are the initial (injected) emittance and the equilibrium emittance respectively, τ_D is the damping time and T is the storage time (200 ms). The initial normalised positron emittance is 0.01 m, and ∼7 damping times (28 ms) are required to achieve the final design normalised emittance of 2×10^{-8} m. The injected electron beam — having been produced by a photoinjector as opposed to a target — has a much better beam quality ($\gamma\varepsilon_i \approx 10^{-5}$ m), and only requires 4 damping times. This provides an opportunity for cost saving by reducing the amount of wiggler in the straight sections, and subsequently reducing the RF power needs.

Energy E	5 GeV
Circumference C	17 km
Hor. extracted emittance $\gamma\varepsilon_x$	8×10^{-6} m
Ver. extracted emittance $\gamma\varepsilon_y$	0.02×10^{-6} m
Injected emittance $\gamma\varepsilon_{x(y)}$	0.01 m (10^{-5} m)
Number of damping times n_τ	7.2 (4.0)
Cycle time T_c	0.2 s
Damping time τ_d	28 ms (50 ms)
Number of bunches n_b	2820
Bunch spacing $\Delta\tau_b$	20×10^{-9} s
Number of particles per bunch N_e	2.0×10^{10}
Current	160 mA
Energy loss/turn	21 MeV (12 MeV)
Total radiated power	3.2 MW (1.8 MW)
Tunes Q_x, Q_y	72.28 , 44.18
Chromaticities ξ_x, ξ_y	-125 , -68
Momentum compaction α_c	0.12×10^{-3}
Equilibrium bunch length σ_z	6 mm
Equilibrium momentum spread σ_p/P_0	0.13 % (0.1 %)
Transverse acceptance $A_{x\|y}$	0.05 m (0.012 m)
Momentum acceptance A_p	1 % (0.5 %)

Table 5.1.1: *Parameters for the TESLA positron damping ring. Where different, values for the electron damping ring are given in parentheses.*

A summary of the main parameters of the damping ring is given in table 5.1.1. Figure 5.1.1 shows a sketch of the positron damping ring, with the long straight section, injection/ejection sections, wigglers, and RF placed in the main linac tunnel. Slight modifications of the arc geometry would allow the wiggler to be placed in the arc tunnel.

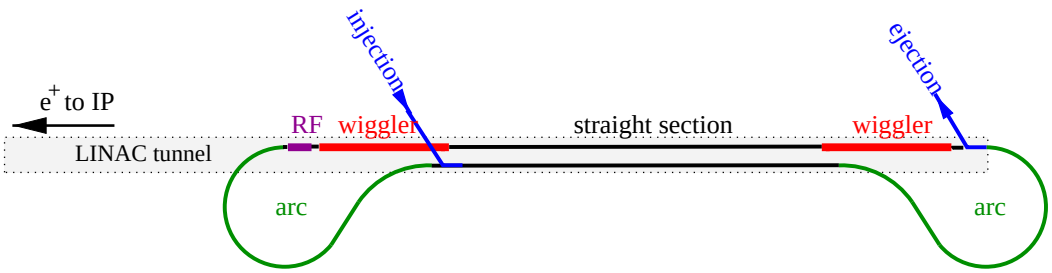

Figure 5.1.1: *Conceptual layout of the positron damping ring. The electron ring is similar with the exception that the injection point is located close to the indicated ejection position at the beginning of the linac.*

The damping ring lattice can be divided into three separate parts:

- the arcs;
- the wiggler sections; and
- the long straight sections in the linac tunnel.

The optics of each of these sections will be described in section 5.2. The investigation of beam dynamics, including space charge effects, dynamic aperture and tolerances, is summarised in section 5.3. Collective effects are discussed following the description of the RF system in section 5.4. Some aspects of the injection and ejection kicker system and basic timing requirements are covered in section 5.5. A summary of the technical layout including detailed drawings of the magnets and vacuum system is given in section 5.6; it also includes the layout of the arc tunnel and a summary of the infrastructure needs of the damping ring.

5.2 Lattice Layout and Optics

5.2.1 Arc lattice

The arc lattice is designed as a minimum emittance cell with a 6° dipole flanked by quadrupole doublets, allowing the phase advance to be changed if desired. The drift space between the two outer focusing quadrupoles provides space for the focusing sextupole at the point of highest horizontal dispersion and β-function. In order to achieve a reasonable bunch length (6 mm), the dipoles are made long (9 m) to increase the momentum compaction factor. The resulting cell length is 15.2 m. In addition, the relatively large cell length results in larger dispersion and β-functions, which reduces the sextupole strength [3].

Figure 5.2.1 shows the optical functions and the geometry of one arc cell. Table 5.2.1 summarises the parameters of the damping ring arcs.

Cell length	15.2 m
Cell phase advance $\mu_x/2\pi$, $\mu_y/2\pi$	0.4 ,0.1
Total number of cells	100
Length of one arc	950 m
Total chromaticity contribution ξ_x, ξ_y	-90 , -35
Total energy loss contribution	1.1 MeV/turn
Total horizontal emittance contribution	2.0×10^{-6} m

Table 5.2.1: *Arc parameters.*

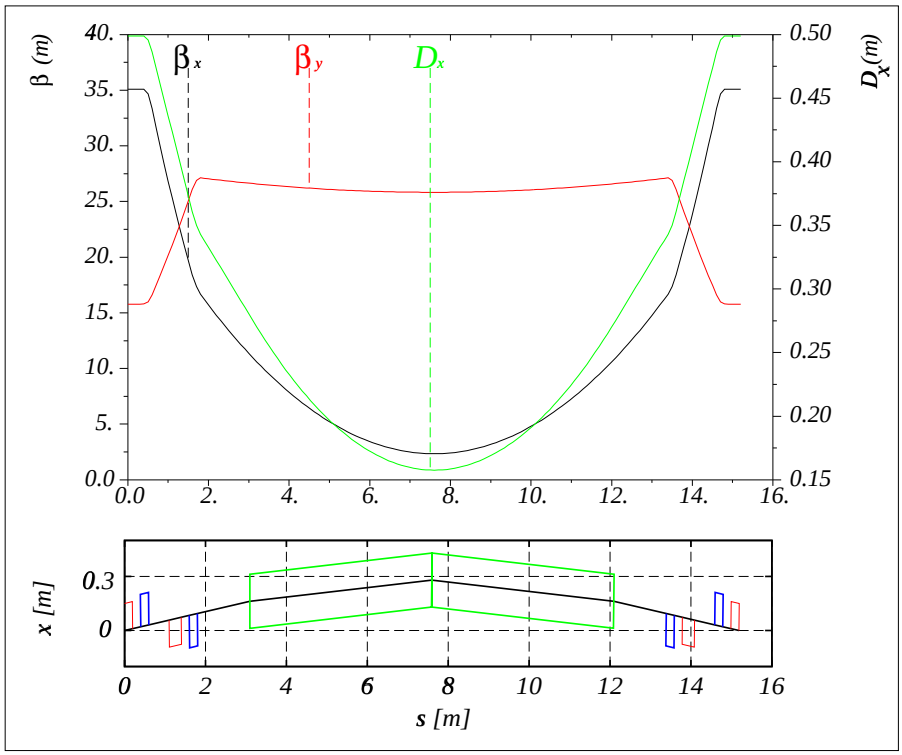

Figure 5.2.1: *Upper plot: horizontal (black), vertical (red) β-functions and horizontal dispersion (green). Lower plot: arc cell geometry showing the location of dipoles (green), quadrupoles (blue) and sextupoles (red).*

5.2.2 Straight section

The long straight section consists of FODO cells of approximately 100 m length with a phase advance of $\mu_{x,y}/2\pi = 0.125$. The choice of both length and phase advance is a compromise between the need to keep the magnet apertures small (smaller β-functions), and a small contribution to the overall chromaticity of the ring (larger β-functions).

The TESLA tunnel follows the curvature of the earth, and thus the straight sections require vertical bending. The emittance contribution of the vertical bending magnets is negligible, but care has to be taken to have no vertical dispersion in the wiggler and arc sections.

Cell length	100 m
Cell phase advance $\mu_x/2\pi$, $\mu_y/2\pi$	0.125, 0.125
Total number of cells	140
Chromaticity contribution ξ_x, ξ_y	−18, −18

Table 5.2.2: *Parameters for the damping ring straight sections.*

Cell length	12.2 m	
Cell phase advance $\mu_x/2\pi$, $\mu_y/2\pi$	0.075 . . . 0.3, 0.125	
Cell chromaticity ξ_x, ξ_y	–0.05 . . . –0.32, –0.14 . . . –0.28	
Maximum vertical beta	18 . . . 28 m	
Energy loss contribution	19.1 MeV/turn	
Radiated power (160 mA)	3 MW	
	Permanent magnet	Electro-magnet
Total number of cells	45	36
Horizontal emittance contribution	$(7.8 \ldots 2.5)\times10^{-6}$ m	$(20.7 \ldots 6.5)\times10^{-6}$ m

Table 5.2.3: *Wiggler section parameters for both electromagnet and permanent magnet designs.*

5.2.3 Wiggler cell

To achieve the desired (positron) damping time of 28 ms, the wigglers have to provide a total second field integral $\int B^2 dl \approx 605\,\mathrm{T^2m}$. Wiggler designs based on electromagnets [2] and permanent magnets [4] have been studied. The basic parameters of the wigglers are given in table 5.6.2. The wigglers can be embedded in either a FODO or triplet focusing lattice, depending on the wiggler length and gap. The final extracted horizontal emittance can be adjusted by changing the average horizontal β-function.

5.3 Beam Dynamics

5.3.1 Space charge effects

The direct space charge force is the collective force of all the particles in the bunch acting on one particle. It is proportional to the particle density in the bunch. The space charge force causes a shift in each particle's tune, leading to an incoherent tune spread within the bunch. With the nominal damping ring parameters the maximum vertical space charge tune shift before ejection (when the beam is smallest) is $\Delta Q_y \approx 0.23$; this relatively large value results primarily from the unusually large ratio of ring circumference to energy, and is one of the reasons for preferring a higher ring energy.

The effect of the large incoherent tune spread has been simulated with the computer code MAD [5], including an extension which simulates the non-linear space charge kicks at each element in the ring [6]. The results suggest that a maximum tune shift of 0.1 is tolerable [7], and hence a reduction of more than a factor of two is required.

Because the long straight sections account for ∼90% of the ring circumference, they are also responsible for the major part of the space charge effects: thus increasing the transverse beam size (i.e. decreasing the charge density) in the straight sections can significantly reduce the incoherent tune shift. Full local transverse coupling in the

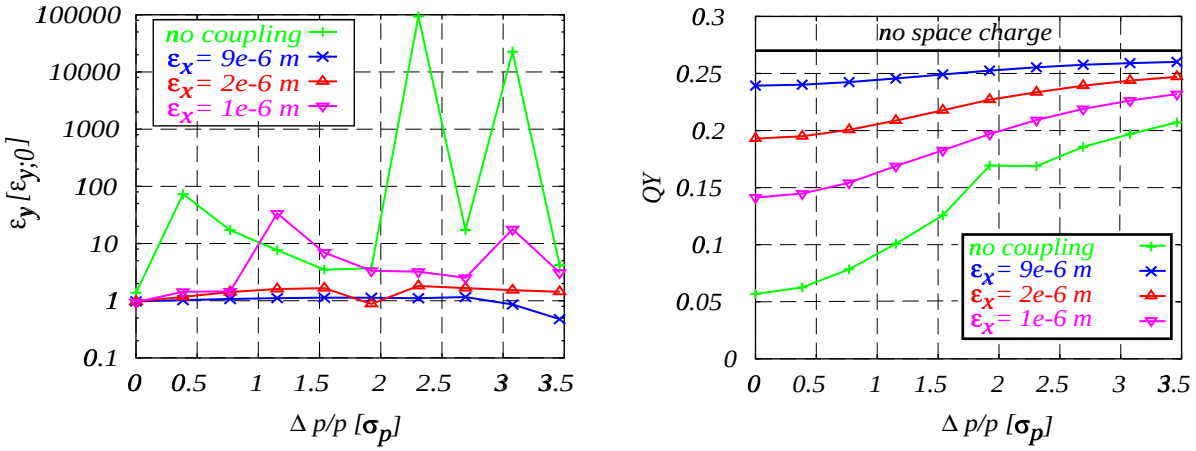

Figure 5.3.1: *Effect of direct space charge force on a single particle in a beam with various horizontal emittances. The test particle performs longitudinal and transverse oscillations with an initial energy offset $\Delta p/p$ and an an initial amplitude corresponding to the nominal vertical emittance. Left: average relative change of vertical action variable (invariant amplitude squared) Right: change of vertical tune.*

straight sections ($\tilde{\varepsilon}_x = \tilde{\varepsilon}_y = \varepsilon_x/2$, where $\tilde{\varepsilon}_{x,y}$ are the *projected* emittances) can reduce the vertical space charge tune shift by as much as a factor of five. The local coupling is provided by two skew-quadrupole insertions placed at the beginning and end of each section.

The effect of the coupling insertion on the beam has been simulated with tracking calculations including space charge forces. The phase and amplitude of a particle was recorded turn by turn under various conditions. The test particle had an initial fractional tune of $\nu_y = 0.27$.

The results for various initial energy offsets ($\Delta p/p$) are shown in figure 5.3.1. With no coupling insertion, the maximum tune (figure 5.3.1 right) shift for the synchronous particle in the centre of the bunch is 0.21 , and the amplitude (figure 5.3.1 left) shows a marked increase when crossing resonances. The coupling insertion reduces the maximum tune shift to 0.035 , and suppresses the amplitude growth. Figure 5.3.1 also indicates that at a maximum tune shift of 0.1 (corresponding to a four times smaller horizontal emittance) only small amplitude growth is observed.

5.3.2 Dynamic acceptance

The dynamic acceptance of the damping ring has been investigated with particle tracking including synchrotron oscillations. Random offsets and roll angles have been given to sextupoles and quadrupoles to simulate realistic optics deviations and coupling. The wiggler has been simulated by an array of hard-edge dipole magnets. The physical aperture of the ring has been simulated in the tracking by applying a maximum transverse amplitude limit.

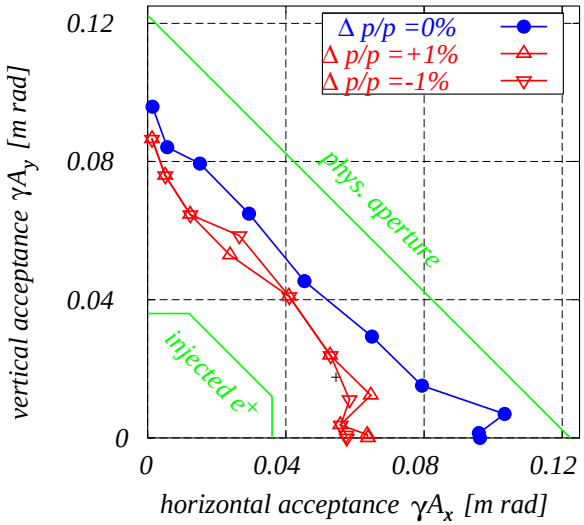

Figure 5.3.2: *Dynamic acceptance of the damping ring. The simulations include quadrupole and sextupole alignment errors which result in an average emittance coupling of* 1 %*, and the real physical aperture as the maximum amplitude limit. The phase space volume of the incoming beam as defined by acceptance of the positron pre-accelerator (see section 4.4) is also shown.*

The dominant source of non-linear beam dynamics are the strong sextupoles in the damping ring arcs; these sextupoles have to provide the chromaticity correction for the complete ring. Multipole errors of the ring magnets can be kept small ($\leq 10^{-3}$ of the design field) by proper design and manufacturing procedures. Sets of particles with various initial ratios of their horizontal and vertical emittances have been tracked over 512 turns (roughly 1 damping time). Two chromatic sextupole families and a second-order dispersion suppressor (to reduces the second-order dispersion in the straight sections) were applied. The results are plotted in figure 5.3.2. The dynamic acceptance achieved is sufficient to accommodate the injected positron beam.

5.3.3 Tolerances

The TESLA damping ring requires a small emittance ratio of 0.2 % at extraction. This ratio has been achieved in present day synchrotron radiation sources and collider rings [8, 9, 10]. Tight alignment tolerances and a high resolution orbit measurement system are crucial.

Vertical emittance is generated through betatron coupling and residual vertical dispersion. Betatron coupling can be reduced with the help of skew-quadrupoles. Minimising spurious vertical dispersion in the wigglers is especially important: here the vertical rms dispersion has to be corrected to the 1 mm level. An algorithm which performs a simultaneous orbit and dispersion correction has been studied. The simulations included alignment errors assigned to all machine elements (as summarised in

Transverse position of elements	0.1 mm
Roll angle	0.2 mrad
BPM resolution	0.01 mm
BPM resolution wiggler section (averaging mode)	0.001 mm

Table 5.3.1: *Alignment tolerances for the damping ring.*

table 5.3.1). Successive steps of the correction algorithm were applied until no further reduction of the residual rms orbit and dispersion were achieved. Studies using many random error seeds showed that the required vertical emittance was obtained on average. Correcting the dispersion to the required 1 mm in the wiggler sections requires a relative orbit measurement with a precision of $\sim 1\mu$m. Beam position monitors (BPM) with a resolution of $10\,\mu$m will be used in the damping ring. For the high-precision dispersion measurement the accuracy can be achieved by averaging.

The dispersion can also be corrected using empirical tuning of the vertical beam size (emittance) with the appropriate dispersion generating orbit bumps; this method has the advantage of not requiring an explicit measurement of the dispersion function.

An important concern is the orbit stability over various time scales. For long-term stability a diffusion-like orbit drift caused by slow uncorrelated ground motion must be taken into account. An orbit correction back to the 'golden' orbit is necessary every few minutes to avoid unacceptable vertical emittance blow-up. For this task a BPM resolution of $10\,\mu$m is sufficient once the vertical emittance has been optimised (i.e. the 'golden' orbit established). On the short time scale the influence of time varying stray fields in the long straight sections is a concern. With no active correction applied to the orbit, the stray field amplitude has to be smaller than a μT. This is in contradiction to measurements on the DESY site, where field amplitudes up to several μT have been observed in typical accelerator environments. Thus a fast orbit feedback has to control the resulting residual orbit in the wiggler and arc sections of the ring.

5.4 RF System and Collective Effects

5.4.1 RF system

The RF System of the damping ring is based upon the following main parameters:

RF Frequency:	500 MHz
Total RF peak voltage:	50 MV
Beam energy loss per turn:	20.3 MeV
Average beam current:	160 mA
Synchrotron radiation power:	3.2 MW

The RF system makes use of 12 superconducting (SC) cavities of the same type developed for CESR [11] and KEK-B [12], and is sketched in figure 5.4.1. Three 1.2 MW

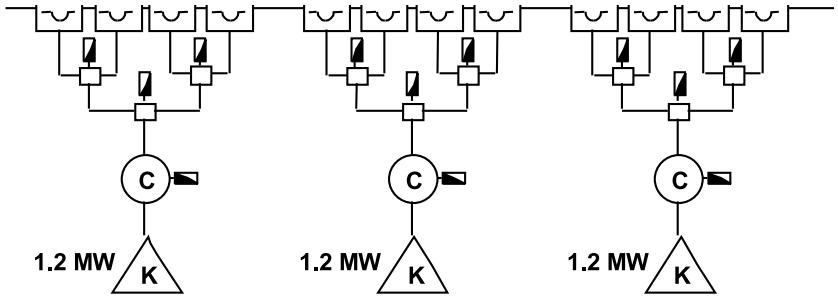

Figure 5.4.1: *Damping ring RF system based on single cell SC cavities.*

klystrons are used.

The SC cavities are single cell Niobium 500 MHz resonators, each housed in its own liquid helium cryostat. Large diameter beam tubes permit the higher order modes (HOMs) to propagate out of the cavities, where they are damped using dissipative material applied to the inner surface of both beam tubes just outside the cryostat at room temperature [13, 14]. Such HOM dampers have been very effective in CESR and KEK-B, and can dissipate up to 10 kW of parasitic power. The quality factor (Q) of the parasitic modes is reduced to a few hundred over the bandwidth 1–3 GHz.

As of writing, the achievable RF field in 500 MHz SC cells is very close to 15 MV/m (i.e. 4.5 MV/cell). To reach these gradients requires high residual resistivity ratio (RRR) Niobium, improved cavity heat treatment and operation at a temperature of 2 K. Twelve cavities would provide up to 54 MV. At 2 K, the cavity Q_0 can be close to 10^{10}. With $R/Q = 45\Omega$ per cell ($R = V^2/2P$), the power loss per cell will be ≤ 30 W at 15 MV/m. The CESR cryostat design, which operates at 4.2 K, has to be re-designed for 2 K operation, where static heat losses of 30 W should be achievable. The total cooling power of 720 MW at 2 K will be provided by the main linac refrigerators.

The 3.2 MW required for the beam will be shared among the twelve cavities, and the input RF power per coupler is therefore 270 kW; this is below the power handling capability (in traveling wave mode) of RF windows already developed and tested at other laboratories [12, 15]. Powerful klystrons (1.2 MW/cw at 500 MHz) are produced by industry and operate routinely at KEK. With a klystron efficiency $\eta \approx 60\,\%$, the total power required by the RF is 6.5 MW.

The heat load for the conventional cooling is mainly the klystron tubes, and is about 2.5 MW. Each cavity cryostat is equipped with a pair of 300 l/s vacuum ion pumps. Two additional 60 l/s pumps are connected to the waveguide power coupler.

5.4.2 Coupled bunch instabilities

The longitudinal and transverse instability growth rates due to the higher-order modes with Q-values of about 100 are of the same order or smaller than the damping rate: therefore a broadband multibunch feedback system may not be necessary, or at least would only require a small damping rate. Multibunch feedback systems with much larger bandwidths than that required for the damping ring are nowadays in routine

Operating frequency	500 MHz
Max RF cavity field	15 MV/m
Cell active length	0.3 m
Number of cavities	12
Total RF voltage	54 MV
RF-to-beam power	3.2 MW
RF cell R/Q	45 Ω
Q_0 at 2 K	$\leq 10^{10}$
Power loss/cell	≤ 30 W
Power per coupler	270 kW
Input coupler Q_{ext}	1.1×10^6
Klystron power	1.2 MW
No. of klystrons	3
Primary power for RF	6.5 MW
Cryostat static losses	≤ 30 W
Cryo-power per cavity	≤ 60 W
Total power at 2 K	≤ 720 W
Water cooling dissipation	2.5 MW

Table 5.4.1: *Damping ring RF system parameters.*

operation in high-current storage rings.

In the transverse plane, coupled bunch instabilities are also strongly driven by the resistive wall effect of the vacuum chamber. The transverse resistive wall impedance of the aluminium vacuum chamber yields $\approx 3200\,\mathrm{M\Omega}$ for the mode number which is equal to the integer part of the transverse tune. This mode gives the largest growth rate of $\approx 2000\,\mathrm{s}^{-1}$. The instability is easily damped with a low-bandwidth feedback.

The interaction of a train of electron bunches with an ion cloud can give rise to a fast single pass coupled bunch instability (Fast Beam Ion Instability [16]). The ion production rate can be estimated based on the residual gas properties and yields upper limits for the allowable vacuum pressure. Computer simulations have shown that the instability is avoided at a nitrogen equivalent pressure of $P_{N_2} \approx 10^{-9}$ mbar [17].

Positron bunches interact with photo-electrons [18, 19, 22]. The creation of electron clouds depends on many parameters, for example: vacuum chamber design and material; external fields; residual gas properties. Electron cloud instabilities have been observed in modern high-current positron storage rings, and can be cured by weak external magnetic fields which confine the photo-electrons to the vacuum chamber surface. The impact of the electron cloud instability on the positron damping ring needs to be investigated in more detail.

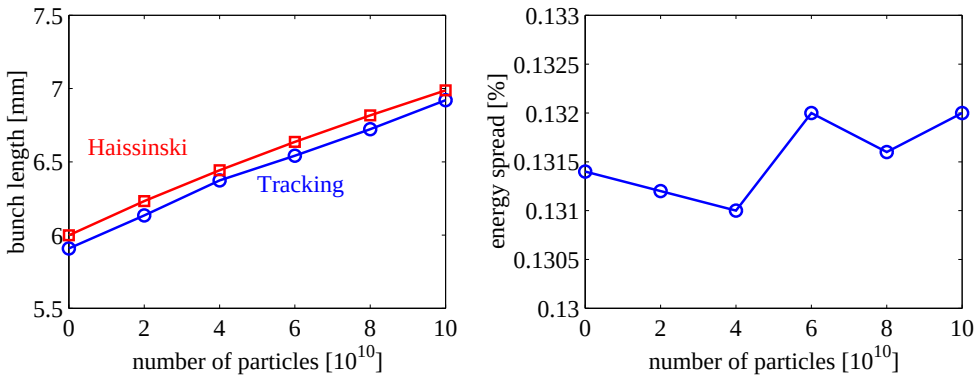

Figure 5.4.2: *Bunch length and energy spread as a function of the number of particles within the bunch. Tracking calculations and Haissinski equation solution are based on the impedance model described in table 5.4.2.*

		$Z_{\|\|}/n$ mΩ	$k_{\|\|}$ V/pC
Non-inductive	RF cavities	2.0	8.8
	Resistive wall	5.4	8.9
	Kickers	≈ 17	≈ 39
	Total	≈ 25	≈ 57
Inductive	Bellows	≈ 11	≈ 3.4
	BPMs	≈ 12.5	≈ 1.7
	Other components	≈ 5	≈ 1.5
	Total	≈ 28.5	≈ 6.6
All components			≈ 64

Table 5.4.2: *Contributions to the longitudinal broadband impedance. $Z_{||}/n$ is the longitudinal impedance divided by the mode number n, and $k_{||}$ the longitudinal loss factor.*

5.4.3 Single bunch effects

The longitudinal single bunch dynamic is influenced by the wakefields generated in the various ring components. Estimates of the different contributions to the impedance budget are given in table 5.4.2.

The effective broadband impedance of the damping ring vacuum system is 25 mΩ, which is below the microwave instability threshold [20] of 61 mΩ. The purely inductive part of the impedance does not contribute to the microwave instability but can lead to bunch lengthening. Tracking calculations in the longitudinal phase space [21] show a bunch lengthening of up to 5 % for an initial bunch length of 6 mm and 2.0×10^{10} particles per bunch (see figure 5.4.2). The energy spread stays constant, indicating the absence of an instability.

The transverse broadband impedance can give rise to the mode-coupling instability. Estimations of the instability threshold and the impedance contributions show that this is of no concern for the damping ring [22].

5.5 Injection and Extraction System

5.5.1 Kicker

The damping ring injection/extraction scheme requires a kicker system with a bandwidth of 50 MHz. The kick strength for both injection and ejection is $\theta \approx 0.6\,\mathrm{mrad}$ or $\int Bdl \approx 0.01\,\mathrm{Tm}$ at 5 GeV and $\beta_{kicker} = 50\,\mathrm{m}$. To ensure an ejected beam stability of $< 0.1\sigma_x$, the amplitude stability of the kicker system has to be $7 \times 10^{-6}\,\mathrm{Tm}$ for both the maximum deflection and the remaining ripple after the kicker pulse; this corresponds to a relative stability of 7×10^{-4} at maximum deflection. Reduction of the relative stability requirement cannot be achieved using (for example) an orbit bump at the ejection septum, since the full aperture of the machine is required for the undamped bunches[1].

A traveling wave kicker showing the required time response has been built and successfully tested [23]. Other concepts like C-yoke kickers around either a sputtered ceramic vacuum chamber or a stripe chamber are under consideration. The necessary pulser technology exists and tests will be performed in 2002. Depending on the chosen kicker/pulser technology, 20–40 kickers are required per ring.

5.5.2 Timing

The timing scheme for the positron damping ring is primarily constrained by the fact that the electron bunches are used to generate the positrons. For the n^{th} 5 Hz pulse, the electron bunches generate the corresponding positron bunches for the next $(n+1)$ pulse: these bunches must be stored in the damping ring, and are injected into the empty bucket created when the corresponding positron bunch for the n^{th} pulse was extracted. This free bucket in the damping ring train must therefore perform 1.5 turns, before being filled again with a new (undamped) bunch.

The positron production scheme leads to the following constraints for the damping ring design and overall collider layout [24]:

- the damping ring circumference, injection position, and harmonic number are fixed;
- the longitudinal position of the main e^+e^- interaction region and the optional second interaction region can only differ by an integer number of half the linac bunch spacing ($\sim$50 m);
- any gap in the damping ring fill (for ion clearing) will be transferred into missing bunches in the linac bunch train.

[1] Damped and undamped bunches are simultaneously present in the ring.

5.6 Technical Layout

5.6.1 Magnets

The damping ring uses conventional water cooled magnets. The main parameters and the number of magnets for each family of the two arcs, wiggler sections and long straight sections of a single damping ring are listed in table 5.6.1. A laminated yoke for both dipoles and multipoles has been foreseen. Bending dipoles and steering magnets have C-shaped cross-sections, while multipole magnets can be split in half to allow easy assembly of the vacuum chamber. The coils have been designed to minimise the power dissipation by keeping the current densities below $2.5\,\mathrm{A/mm^2}$. Figure 5.6.1 shows a bending magnet while figure 5.6.2 shows a typical quadrupole and sextupole. Two-dimensional codes for basic dimensioning of all the magnets have been used: however the design of the pole profiles needs further optimisation to minimise the non-linear magnetic fields. The mechanical length of each type of magnet has been scaled from experience. Detailed three-dimensional simulations must be performed to set the final dimensions.

Special girders, where magnets, vacuum chambers and pumps, etc. are assembled and carefully aligned outside the tunnel, have been designed to reduce the installation time inside the tunnel.

Two alternative designs for the damping wigglers have been studied: permanent magnet [4] and electromagnetic technology. A schematic view of the permanent magnet wiggler is shown in figure 5.6.3; its advantages are compact size and low operating costs. On the other hand, an electromagnetic wiggler is tunable and less sensitive to radiation damage. The specific design of the electromagnetic wiggler magnet is shown in figure 5.6.4. Due to cost and space constraints, the maximum current density is limited to $8.6\,\mathrm{A/mm^2}$. The power requirements for the electromagnetic wiggler is 6.8 MW, corresponding to 85 % of the total power required by all the magnets. Therefore the permanent magnet wiggler has been chosen as the reference design for the damping ring. Radiation damage will be avoided by means of collimation and an active protection system.

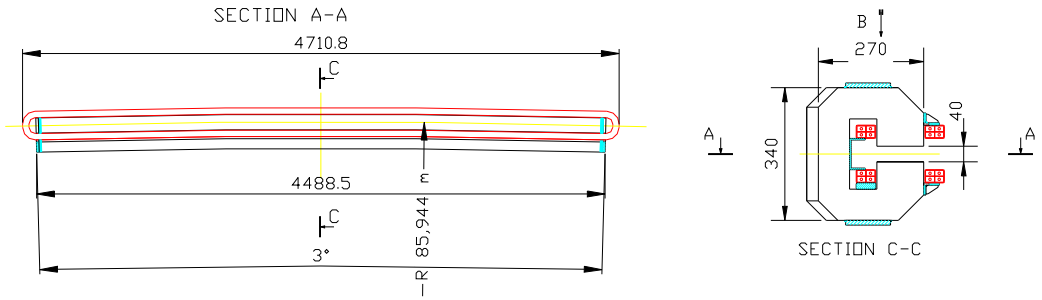

Figure 5.6.1: *Bending magnet.*

Bending magnets	Quantity	Mag. length [m]	Defl. angle [deg]	Mag. field [T]	Gap [mm]	Ampere turns [A]	Power/ magnet [W]
	216	4.5	3	0.194	40	6176	2557

Quadrupoles	Quantity	Mag. length [m]	Max. gradient [T/m]	Bore radius [mm]	Ampere turns/pole [A]	Power/ magnet [W]
Arc	456	0.2	21.7	24	4973	631
Arc match	38	0.3	10.3	24	2361	258
Wiggler	70	0.2	14.2	18	3254	270
Wiggler match	16	0.4	10.9	28	3400	270
Long straight	269	0.2	7.5	52	8070	1085

Sextupoles	Quantity	Mag. length [m]	Max. gradient [$\mathrm{T/m^2}$]	Bore radius [mm]	Ampere turns/pole [A]	Power/ magnet [W]
SF	204	0.3	101.7	24	187	46
SDA	96	0.4	130.1	24	240	78
SDB	12	0.2	130.1	24	240	43

Steering magnets	Quantity	Mag. length [m]	Nom. field [T]	Gap [mm]	Ampere turns [A]	Power/ magnet [W]
Arc, wiggler	360	0.1	0.08	120	8620	190
Long straight	269	0.1	0.003	105	288	2

Table 5.6.1: *Damping ring magnet parameters.*

Wigglers	Quantity	Period length [mm]	# of periods	Max. Field [T]	$\frac{\int B^2 dl}{L}$ $\left[\frac{\mathrm{T^2 m}}{\mathrm{m}}\right]$	Gap [mm]	Ampere turns/ pole [A]	Power/ magnet [W]
Electro-magnetic	72	550	8	1.8	2.1	25	20500	94000
Permanent magnet	90	400	12	1.67	1.37	25		

Table 5.6.2: *Wiggler magnet parameters for both the electromagnetic and permanent magnet wiggler.*

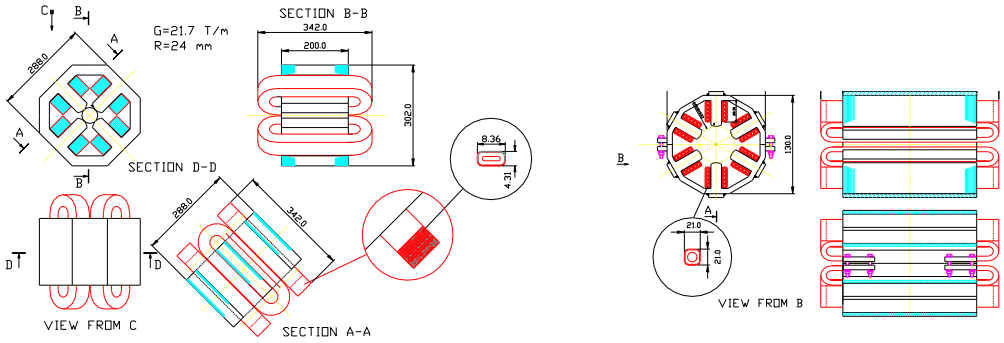

Figure 5.6.2: *Typical quadrupole magnet (left) and sextupole magnet (right).*

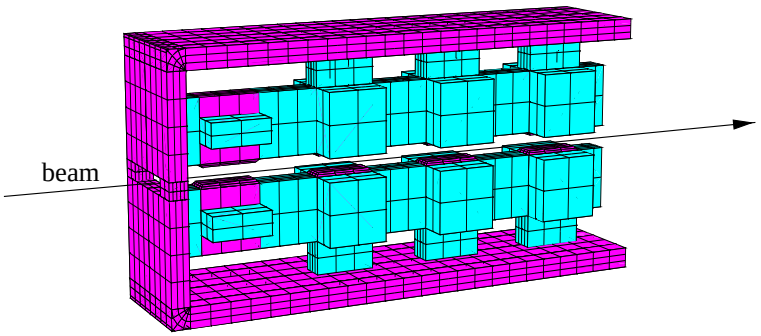

Figure 5.6.3: *Partial view of the permanent magnet wiggler. The permanent magnet material is drawn in blue and the iron poles and yoke in magenta. The side yoke plates which enclose the whole structure are not shown.*

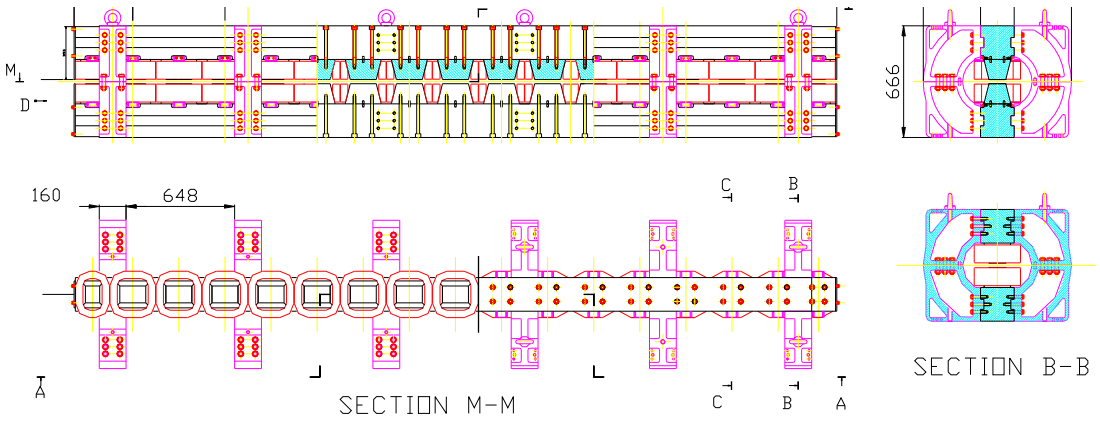

Figure 5.6.4: *Electromagnetic wiggler.*

5.6.2 Vacuum system

The vacuum system has been designed to achieve a mean pressure inside the vacuum chamber of $\sim 10^{-8}$ mbar in the arc sections, and $\sim 10^{-9}$ mbar in the long straight sections.

5.6.2.1 Residual gas sources

The residual gas inside the vacuum chamber has a contribution from two sources: thermal out-gassing and synchrotron radiation photo-desorption. The thermal out-gassing contribution is proportional to the inner surface of the vacuum chamber and strongly depends on the surface condition and treatment. A reasonable estimate of the thermal gas load is in the range from 10^{-10} to 10^{-11} mbar l/s cm^2 for a well cleaned surface. The synchrotron radiation photo-desorption contribution is proportional to the photon flux emitted by the particle beam, and is a function of the beam dose.

The synchrotron radiation properties of the dipole and wiggler are given in table 5.6.3. After a beam dose of about 50 Ah, it is reasonable to consider a desorption coefficient of about 3×10^{-6} molecules per photon. The total gas load contributions are given in table 5.6.4.

	Dipole	Wiggler	
Photon flux at 160 mA	5.4×10^{18}	3×10^{19}	photons/magnet/s
Synchrotron radiation power	860	34	kW/magnet
Maximum surface power density	190	1	kW/mm^2

Table 5.6.3: *Synchrotron radiation properties for dipoles and wigglers.*

Thermal	6×10^{-4}	mbar l/s
Dipole	1.3×10^{-4}	mbar l/s
Wiggler	1.2×10^{-4}	mbar l/s

Table 5.6.4: *Contributions to the total gas load.*

5.6.2.2 Vacuum chamber

The vacuum chamber in the bending magnets (see figure 5.6.5) accommodates a distributed pumping system. A suitable RF screen will be used to separate the beam channel from the pumping chamber. A cooling channel is present to remove the synchrotron radiation power load. In the straight sections between dipoles, the vacuum chamber is circular with a cooling channel on one side (see figure 5.6.5). In the two 7 km long straight sections the vacuum chamber is essentially a pipe of 100 mm outside diameter and 2 mm thickness, and no cooling is needed. In the wiggler sections, the

vacuum chamber has a central beam channel and two ante-chambers (see figure 5.6.6), where the synchrotron radiation fan travels before being stopped by absorbers. The vacuum chamber inside the quadrupole has a cross section as shown in figure 5.6.6. Downstream of each wiggler is a water cooled synchrotron radiation absorber with a pumping station, as shown in figure 5.6.7. All vacuum chambers are constructed from an aluminium alloy.

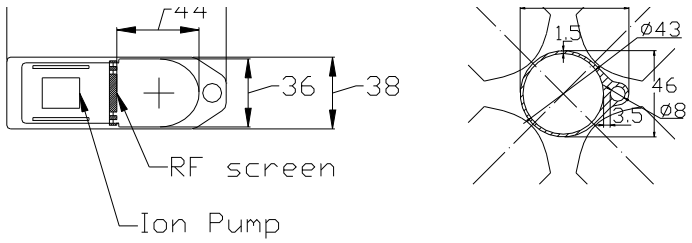

Figure 5.6.5: *Dipole vacuum chamber with distributed ion pump (left), and quadrupole vacuum chamber (right).*

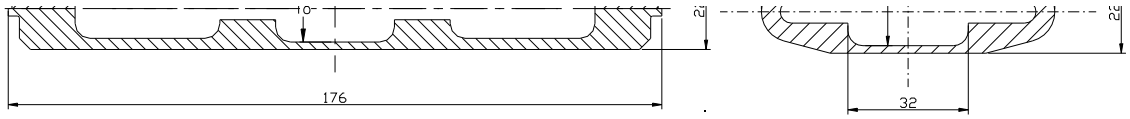

Figure 5.6.6: *Wiggler vacuum chamber with ante-chamber (left), and wiggler cell quadrupole vacuum chamber (right).*

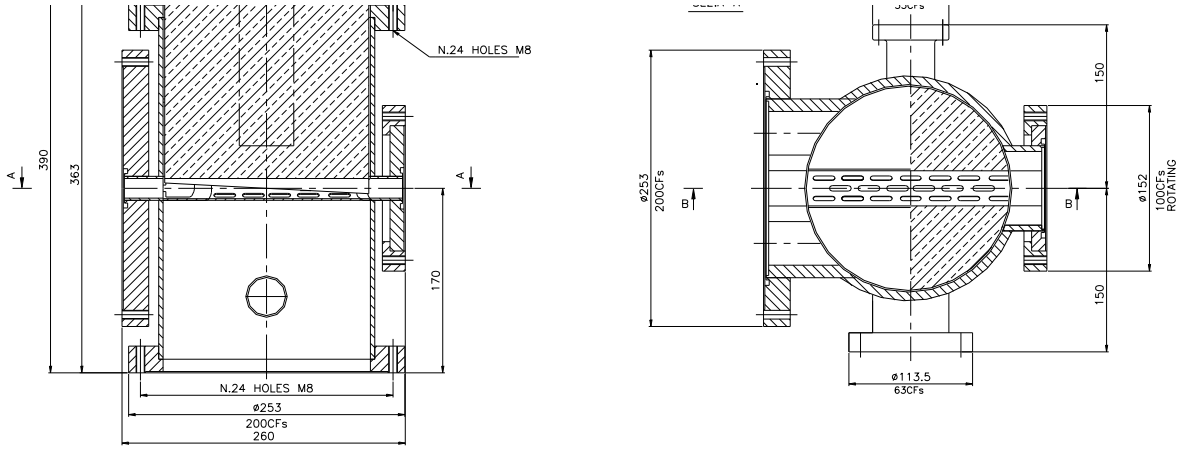

Figure 5.6.7: *Synchrotron radiation absorber.*

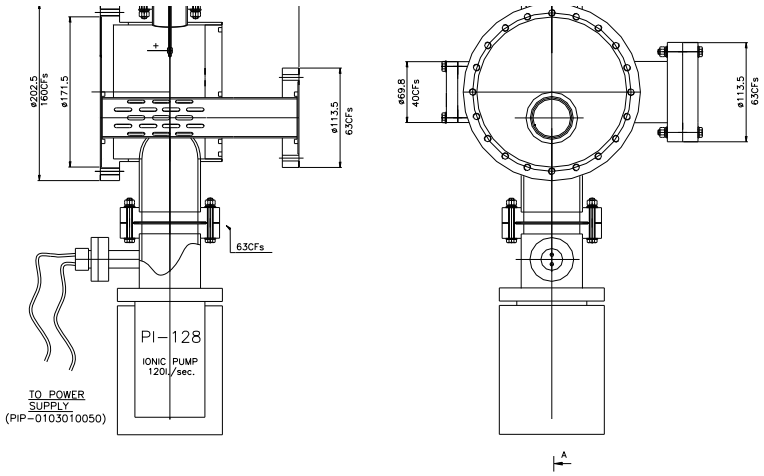

Figure 5.6.8: *Typical pumping station.*

5.6.2.3 Vacuum pumps

Table 5.6.5 lists the pumps required for the damping ring. The lumped vacuum pumps are connected to the chamber by means of a special RF-screened vacuum port (figure 5.6.8). The section has two flanges to connect the pump and a vacuum gauge, and a third flange which connects to a valve used during pump down.

Location	Quantity	Item	Pumping rate [l/s]
Arcs	216	distributed sputter ion pumps	190
	368	lumped sputter ion pumps	120
Wigglers	72	lumped sputter ion pumps	400
RF cavities	24	lumped sputter ion pumps	400
Long Straights	1876	titanium sublimation pumps	1000
	1876	lumped sputter ion pumps	60

Table 5.6.5: *Required pump installation.*

5.6.2.4 Bellows

Installed on the arc vacuum chambers are 662 bellows with a 43 mm inside diameter. The vacuum chamber for the long straight sections contains 1876 bellows with a 96 mm inside diameter (see figure 5.6.9). Each bellow is provided with a sliding contact RF screen.

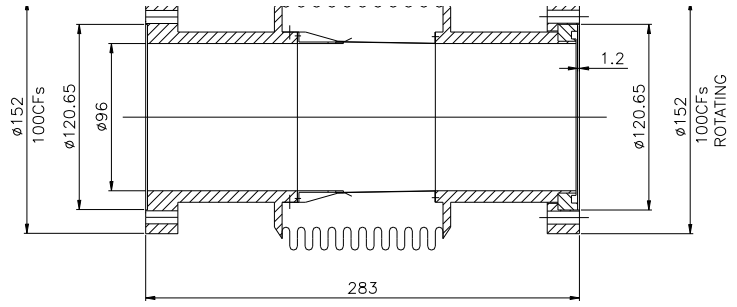

Figure 5.6.9: *RF screened bellows.*

5.6.2.5 Gate valves

Electro-pneumatic all-metal gate valves with RF contact are used to section the vacuum chamber. The number, type and location of the valves are given in table 5.6.6.

Location	Quantity	Item
Arcs	30	electro-pneumatic gate valves DN 63 with RF contact
Long Straight	60	electro-pneumatic gate valves DN 100 with RF contact
RF section	6	electro-pneumatic gate valves DN 200 with RF contact

Table 5.6.6: *Location, type and number of vacuum valves required.*

5.6.3 Infrastructure

5.6.3.1 Arc tunnel layout

The damping ring arc is located in a tunnel with 3 m inner diameter (see figure 5.6.10). This tunnel is connected at two positions to the main linac tunnel.

Each arc is equipped with a monorail transportation system capable of transporting material, components and people as shown in figure 5.6.10. The components are directly hung on the rail axis while people and generic materials can be carried on a trolley running on the tunnel side-walk. The system is powered by sliding contacts at 400 V. The main characteristics of the transportation system are:

Velocity:	5–50 m/min
Monorail loading capacity:	10 t (5 t per crane)
Trolley loading capacity:	4 people plus 1500 kg
Transversal stroke:	±100 mm on the tunnel axis

Additional infrastructure in the arcs consists of:

- a compressed air distribution line running along the whole arc;

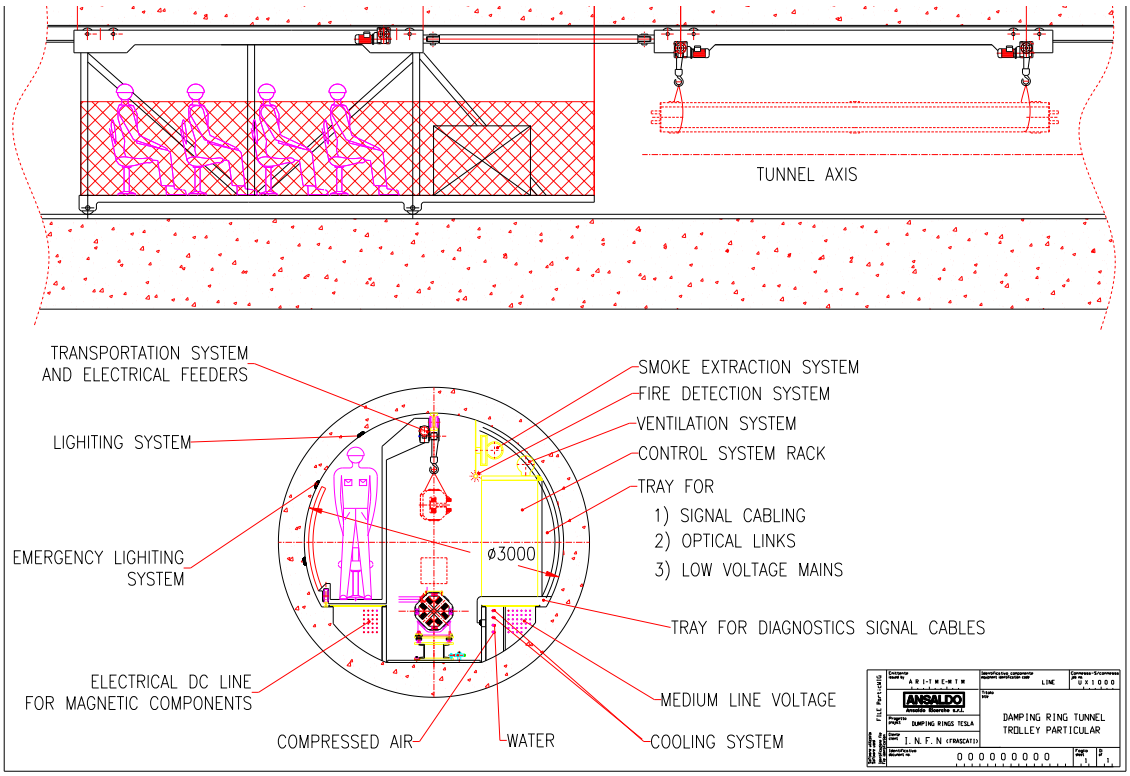

Figure 5.6.10: *Arc tunnel cross section.*

- a fire detection and extinguishing system;
- normal and emergency lighting, and an optical video circuit;
- a ventilation and air extraction system.

5.6.3.2 Electrical services and cooling systems

The electrical power needs for the damping rings are summarised in table 5.6.7, while the conventional cooling system requirements are summarised in table 5.6.8 (the cooling capacity of 720 MW for the superconducting RF cavities will be provided by the main linac refrigerators). More detailed information can be found in sections 8.4 and 8.5. The electron damping ring needs less damping (see section 5.1), i.e. the total power loss due to synchrotron radiation is smaller. Consequently the electric power consumption of the RF system and the cooling capacity are reduced.

	Positron ring	Electron ring
RF klystrons	6.5 MW	4.3 MW
Magnet power supplies	2.0 MW	
Other systems	0.5 MW	
Total	9.0 MW	6.8 MW

Table 5.6.7: *Electrical power needs of damping ring systems.*

	Positron ring	Electron ring
RF klystrons	3.3 MW	2.2 MW
Synchrotron radiation	3.2 MW	2.1 MW
Magnets and power supplies	2.0 MW	
Total	8.5 MW	6.3 MW

Table 5.6.8: *Cooling capacity for damping rings.*

Bibliography

[1] K. Flöttmann, J. Rossbach, *Emittance Damping Considerations for TESLA*, DESY 93-023, 1993.

[2] C. Sanelli et. al., *Technical Layout of the TESLA Damping Ring*, LNF-01/003 (IR), 2001.

[3] W. Decking, *Optical Layout of the TESLA 5 GeV Damping Ring*, DESY TESLA-01-11, 2001.

[4] M. Tischer, J. Pflüger, W. Decking, *A Permanent Magnet Wiggler Design for the TESLA Damping Ring*, DESY TESLA-00-20, 2000.

[5] H. Grote, F. Iselin, *The MAD Program*, CERN/SL/90-13(AP), 1996.

[6] F. Ruggiero, F. Zimmermann, *Consequences of the Direct Space Charge Effect for Dynamic Aperture and Beam Tail Formation in the LHC*, Proc. Part. Acc. Conf., New York 1999, p. 2626.

[7] W. Decking, R. Brinkmann, *Space Charge Problems in the TESLA Damping Ring*, Proc. 7^{th} EPAC, Vienna 2000, p. 1024.

[8] R. Nagaoka, *Work Carried Out at the ESRF to Characterise and Correct the Coupling*, Proc. 7^{th} EPAC, Vienna 2000, p. 131.

[9] E.B. Blum, *Operation of a Low Emittance Lattice at the NSLS X-RAY Ring*, Proc. Part. Acc. Conf., New York 1999, p. 2304.

[10] M. Zobov, *Status Report on DAΦNE Performance*, Proc. 7^{th} EPAC, Vienna 2000, p. 43.

[11] E. Chojnacki, J. Sears, *Superconducting RF Cavities and Cryogenics for CESR III Upgrade*, Cornell SRF 990716-09, 1999.

[12] T. Tajima et al., *The Superconducting Cavity System for KEKB*, Proc. Part. Acc. Conf., New York 1999, p. 440.

[13] T. Tajima et al., *Development of HOM Damper for B-Factory (KEKB) Superconducting Cavities*, KEK Preprint 95-77, 1995.

[14] S. Belomestnykh et al., *Comparison of the Predicted and Measured Loss Factor of the Superconducting Cavity Assembly for the CESR Upgrade*, Cornell SRF 950406-04, 1995.

[15] E. Chojnacki et al., *Tests and Designs of High-power Waveguide Vacuum Windows at Cornell*, Part. Accel. **61** (1998) 309.

[16] T.O. Raubenheimer and F. Zimmermann, *A Fast Beam - Ion Instability in Linear Accelerators and Storage Rings*, SLAC-PUB-95-6740 and Phys. Rev. **E 52** (1995) 5487.

[17] C. Montag, *Simulation of the Fast Beam-Ion Instability in the TESLA Electron Damping Ring*, DESY TESLA-00-16, 2000.

[18] K. Ohmi, *Beam-Photoelectron Interactions in Positron Storage Rings*, Phys. Rev. Lett. **75:8** (1995) 1526.

[19] K. Ohmi and F. Zimmermann, *Head-Tail Instability Caused by Electron Clouds in Positron Storage Rings*, Phys. Rev. Lett. **85:18** (2000) 3821.

[20] A. Chao, *Physics of Collective Beam Instabilities in High Energy Accelerators*, John Wiley & Sons Inc., 1993.

[21] C. Burnton, *Tracking Studies in the Longitudinal Phase Space for the TESLA Damping Ring Design*, DESY TESLA-98-15, 1998.

[22] V.D. Shiltsev, *TESLA Damping Ring Impedances: Preliminary Design Considerations*, DESY TESLA-96-02, 1996.

[23] B.I. Grishanov, F.V. Podgorny, J. Ruemmler, V.D. Shiltsev, *Very Fast Kicker for Accelerator Applications*, DESY TESLA-96-11, 1996.

[24] W. Kriens, *Basic Timing Requirements for TESLA*, DESY TESLA-01-10, 2000.